**University of Bath**

# Darcy-Bénard-Bingham Convection

D. A. S. Rees

*Department of Mechanical Engineering, University of Bath, Bath BA2 7AY, UK*

The present paper is the first to consider Darcy-Bénard-Bingham convection. A Bingham fluid saturates a horizontal porous layer which is subjected to heating from below. It is shown that this simple extension to the classical Darcy-Bénard problem is linearly stable to small-amplitude disturbances but nevertheless admits strongly nonlinear convection. The Pascal model for a Bingham fluid occupying a porous medium is adopted, and this law is regularized in a frame-invariant manner to yield a set of two-dimensional governing equations which are then solved numerically using finite difference approximations. A weakly nonlinear theory of the regularized Pascal model is used to show that the onset of convection is via a fold bifurcation. Some parametric studies are performed to show that this nonlinear onset of convection arises at increasing values of the Darcy-Rayleigh number as the Rees-Bingham number increases, and that for a fixed Rees-Bingham number the wavenumber at which the rate of heat transfer is maximised increases with the Darcy-Rayleigh number.

Keywords: Porous media, Bingham fluid, convection, stagnation, nonlinear onset, fold bifurcation.

## I. INTRODUCTION

Free convective motions which are induced by heating a uniform horiontal layer of fluid from below is known as Rayleigh-Bénard convection and it is one of the most widely-studied fluid mechanical problem which involves instability. Applications of convecting systems of this type, which show a close relationship with the Rayleigh-Bénard problem, may be found in nature; these include the modelling of the outer core of the earth, the presence of granulation on the surface of the sun, the study of $CO_2$ sequestration and the instability of evolving dense boundary layers, the modelling of instabilities in solar ponds, and the description of the mechanisms behind patterned ground formation. The present paper is concerned with how the well-known stability properties of the Rayleigh-Bénard problem are modified when a Bingham fluid saturates a porous medium.

When the porous matrix is absent, and if the layer of fluid is uniform in every respect, then the basic state which persists consists of a linear drop in temperature between the upper and lower surfaces together with a motionless fluid. Given that a Bingham fluid requires a finite body force of some kind (e.g. pressure gradient, buoyancy forces) this means that any small-amplitude perturbation, such as a local temperature disturbance, will diffuse and decay. Therefore the layer is linearly stable. However, it remains possible for large-amplitude convection to arise and to persist. There are now many authors who have considered these matters. Because of the absence of a linear stability theory, the great majority of these authors have resorted to computational analysis.

In a remarkable pioneering paper Zhang et al.[1] performed energy stability analyses and nonlinear computations in order to provide a comprehensive analysis of what might be called the Rayleigh-Bénard-Bingham problem. They also derived estimates for the decay rates of disturbances and found that there is a sudden transition to the zero-flow state as the Rayleigh number is reduced, which is consistent with the lack of a linear stability threshold. Later, experimental works were undertaken by Darbouli et al.[2] and Kebiche et al.[3] using Carbopol solutions to mimic a Bingham fluid. Despite careful experimental procedures it is clear from these works that certain important aspects of the theoretical problem are not realised in the experiments; these include the appearance of an imperfect bifurcation rather than a fold bifurcation to the strongly convecting regime. In addition, the presence of surface slip due to having surfaces of different roughnesses may explain quantitative differences between these two experimental works. We also mention the more recent work by Metivier et al.[4]. Further numerical works by Turan et al.[5–7] and Yigit et al.[8–10] are devoted much more to the devising of analytical correlations for the Nusselt number, and to a presentation of the evolution of unyielded regions within the cavities.

In the present paper we are concerned with the porous medium analogue of the Rayleigh-Bénard-Bingham problem which we shall call the Darcy-Bénard-Bingham problem. There are very few works which are devoted to the convective motion of Bingham fluids when they saturate a porous medium. Most of these are boundary layer flows; see Rees[11] for a discussion of these works. A series of four papers by Rees and Bassom[12–15] is devoted to different aspects of one-dimensional flows and it covers similar ground to works by Yang and Yeh[16], Kleppe and Marner[17], Patel and Ingham[18], Bayazitoglu et al.[19] and Barletta and Magyari[20]. Rees[21] has also presented nonlinear computations for convection in a sidewall-heated cavity and found that the presence of a Bingham fluid means that there is a critical value of the Darcy-Rayleigh number above which convection arises. The numerical evidence presented there suggests that that critical value is precisely the product of a suitable-defined porous Bingham number and the length of the perimeter of the cavity. Here, we shall find, perhaps not surprisingly in view of the above brief discussion of the Rayleigh-Bénard-Bingham problem, that convection needs to be initiated by disturbances with large amplitude and that the motionless basic state is linearly stable.

To this end we will describe in some detail the numerical scheme which we have adopted. Beginning with the piecewise-linear model of Pascal[22] which shows a threshold pressure gradient, a regularization is introduced in order to be able to apply standard methods of numerical solution. These matters are covered in Section 2. In Section 3 we

present some sample solutions, a detailed weakly nonlinear analysis of the regularised Pascal model, and numerically-sourced information about (i) how the presence of the yield threshold alters the strength of convection, (ii) the value of the Darcy-Rayleigh number at which convection first appears, (iii) the range of wavnumbers for which convection exists and (iv) the wavenumber which maximises the mean Nusselt number. Some further discussion and conclusions follow in Section 4.

## II. GOVERNING EQUATIONS

### A. Pascal's law.

The mean speed at which a Bingham fluid moves through a porous medium depends quite strongly on the microstructure of the medium. For example, if the porous medium is composed of parallel tubes or channels, then the well-known Buckingham-Reiner law (Buckingham[23], Reiner[24]) may be used to provide one version of what might be termed a Darcy-Bingham law. There will exist a threshold pressure gradient above which the fluid flows. Once that threshold is exceeded, then the dependence of the flow rate on the excess pressure gradient is quadratic at first, but asymptotes to a linear dependence at larger pressure gradients. Such a dependence was described by Bingham[25], although he attributed the curved part of the velocity dependence to leakage in the experiments. The presence of a distribution of channels softens further the initial flow rate dependence on the excess pressure gradient; see Nash and Rees[26]. Thus it is inferred that there is no definitive Darcy-Bingham law, but a detailed analysis or set of experiments is required to find the appropriate one for each microstructure.

However, experimental work by Pascal[22], who considered the unidirectional flow of an isothermal fluid, showed that Darcy's law may be modified into a piecewise-linear dependence of the velocity on the applied pressure gradient:

$$
u = \begin{cases} \dfrac{K}{\mu}\left(-\dfrac{dp}{dx} - G\right) & -\dfrac{dp}{dx} > G, \\[2mm] 0 & \text{otherwise} \\[2mm] \dfrac{K}{\mu}\left(-\dfrac{dp}{dx} + G\right) & -\dfrac{dp}{dx} < -G. \end{cases} \tag{1}
$$

This is shown as the dashed line in figure 1, while the familiar Darcy's law for a Newtonian fluid is the continuous line. This expression is sometimes known as Pascal's law and the value, $G$, is the threshold pressure gradient.

Equation (1) may be seen to serve as a good approximation to the actual flow/pressure-gradient relationship for a general porous microstructure except for close to the threshold itself (Nash and Rees[26]). Bingham's original experimental work (Bingham[25]) mimics well the Buckingham-Reiner law, where the discontinuity in slope at the threshold gradient is replaced by a smooth transition. For reference, we mention that the
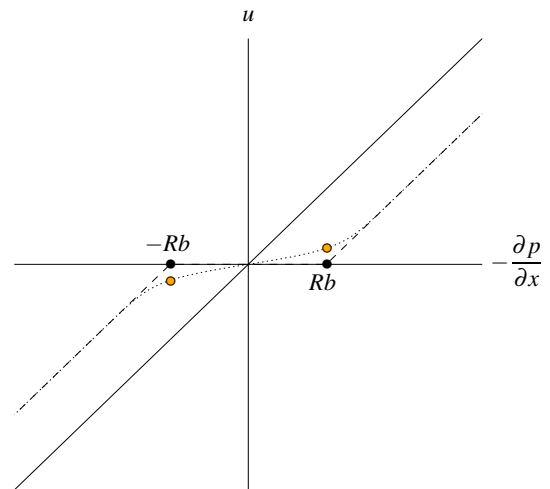


FIG. 1. The dependence of the induced velocity on the applied pressure gradient for Darcy's law (continuous), the Pascal[22] threshold model (dashed), and our regularized form of the threshold model (dotted) when $c = 5$. The black disks represent the range of values of the pressure gradient for which the medium is stagnant. The orange disks indicate the corresponding range of velocities for which the medium is deemed to be stagnant.

threshold gradient may be found easily to be given by

$$
G = \frac{2\tau_0}{h} \tag{2}
$$

when the porous medium consists of identical unidirectional channels of of width, $h$ (Nash and Rees[26]), where $\tau_0$ is the yield stress of the fluid, and only quantitative changes are found when considering uniform pipes with different cross-sectional profiles.

We shall now assume that it is possible to extend Pascal's model to an isotropic two-dimensional form. Presently unpublished work by the present author shows that there is an anisotropic response of the fluid to changes in the orientation of an applied pressure gradient for square, triangular and hexagonal networks of identical channels. All three of these configurations are isotropic when the fluid is Newtonian, and therefore our present assumption is that a suitably random network of channels will be required to give an isotropic momentum equation for a Bingham fluid. We shall therefore extend Eq. (1) to the following two-dimensional form:

$$
\begin{pmatrix} u \\ w \end{pmatrix} = \begin{cases} -\dfrac{K}{\mu}\left[1 - \dfrac{G}{(p_x^2 + p_z^2)^{1/2}}\right] \begin{pmatrix} p_x \\ p_z \end{pmatrix} & \text{if } p_x^2 + p_z^2 > G^2, \\[4mm] \begin{pmatrix} 0 \\ 0 \end{pmatrix} & \text{otherwise,} \end{cases} \tag{3}
$$

which may be seen to be frame-invariant. Given that the present paper is concerned with the onset of convection, it is necessary to include buoyancy as another body-force term.

Subject to the Boussinesq approximation Eq. (3) becomes,

$$\binom{u}{w} = \begin{cases} -\dfrac{K}{\mu}\left[1-\dfrac{G}{B}\right]\begin{pmatrix} p_x \\ p_z - \rho g \beta(T-T_c) \end{pmatrix} & \text{if } B > G, \\[2ex] \begin{pmatrix} 0 \\ 0 \end{pmatrix} & \text{otherwise,} \end{cases}$$

(4)

where $B = \sqrt{p_x^2 + (p_z - \rho g \beta(T-T_c))^2}$, and where $z$ is the vertical coordinate. This extension of Eq. (3) to the form given in Eq. (4) is based on the observation that $p_x$ and $p_z$ represent the body forces acting in the $x$ and $z$-directions, respectively, in Eq. (3), while those roles are played by $p_x$ and $p_z - \rho g \beta(T-T_c)$, respectively, in Eq. (4). The full set of governing equations is completed by the equation of continuity,

$$u_x + w_z = 0,$$

(5)

and the heat transport equation,

$$\sigma T_t + u T_x + w T_z = \alpha(T_{xx} + T_{zz}),$$

(6)

where $\sigma$ is the heat capacity ratio and $\alpha$ is the thermal diffusivity of the porous medium. The boundary conditions are that,

$$w = 0, \; T = T_h \quad \text{on } z = 0 \quad \text{and} \quad w = 0, \; T = T_c \quad \text{on } z = d,$$

(7)

and that

$$u = 0, \; \theta_x = 0 \quad \text{on both} \quad x = 0 \; \text{and} \; x = Ad,$$

(8)

where $A$ is the aspect ratio of the cavity.

**B. Scalings**

The aim of the paper is to present computations of the effect of the presence of a yield stress on nonlinear convection in a porous layer heated from below. The natural lengthscale is the height of the layer, $d$. Consequently we may introduce the following scalings,

$$(x,z) \to d(x,z), \quad (u,w) \to \frac{\alpha}{d}(u,w), \quad p \to \frac{\mu \alpha}{K} p,$$

(9)

$$T = T_c + \theta(T_h - T_c), \quad t \to \frac{\sigma \alpha}{d^2} t.$$

(10)

The governing equations now take the forms,

$$u_x + w_z = 0,$$

(11)

$$\binom{u}{w} = \begin{cases} -\left[1 - \dfrac{Rb}{\sqrt{p_x^2 + (p_z - Ra\,\theta)^2}}\right]\begin{pmatrix} p_x \\ p_z - Ra\,\theta \end{pmatrix} \\ \qquad \qquad \text{if } \sqrt{p_x^2 + (p_z - Ra\,\theta)^2} > Rb, \\[2ex] \begin{pmatrix} 0 \\ 0 \end{pmatrix} \\ \qquad \qquad \qquad \text{otherwise.} \end{cases}$$

(12)

$$\theta_t + u \theta_x + w \theta_z = \theta_{xx} + \theta_{zz}.$$

(13)

The full nondimensional system is seen to be governed by the Darcy-Rayleigh and the Rees-Bingham numbers, and these are,

$$Ra = \frac{\rho g \beta K H(T_h - T_c)}{\mu \alpha}, \qquad Rb = \frac{GKH}{\mu \alpha}.$$

(14)

The latter may be described as a porous thermal Bingham number because of the presence of the yield threshold, $G$, the permeability, $K$ and the thermal diffusivity, $\alpha$, and therefore it is an appropriate parameter for describing the effects of a yield threshold on the convective flow of a Bingham fluid in a porous medium; see Rees[11]).

**C. Regularization.**

Equation (12) is not in a form which is suitable for the application of standard numerical methods. Indeed, even in the unidirectional form given in Eq. (1) it cannot be used to simulate Bingham fluid flows because the pressure gradient cannot be regarded as a single-valued function of the induced flow. Therefore we choose to regularise Eq. (1) (or rather, its nondimensional version) in order to demonstrate the technique, and then to apply the same idea to the two-dimensional Eq. (12).

After scaling, (1) takes the form,

$$u = \begin{cases} -\left[1 - \dfrac{Rb}{|p_x|}\right] p_x & \text{if } |p_x| > Rb, \\[2ex] 0 & \text{otherwise,} \end{cases}$$

(15)

and we may introduce the following regularised form,

$$u + Rb \tanh(cu/Rb) = -p_x,$$

(16)

where $c$ is the regularization constant. Equation (16) clearly defines the pressure gradient as a single-valued function of velocity, and therefore it may be used for computation. Although Eqs. (15) and (16) look quite different, a comparison of the two is given in figure 1 where $c = 5$ has been used. When $c$ takes larger values than this then the curves match increasingly closely. Equation (16) replaces the pure Pascal model by a pseudoplastic fluid with an effective viscosity which is $(1+c)\mu$ when the fluid velocities are small, and a plastic viscosity which is equal to $\mu$ at much higher rates of flow. It is possible to interpret this regularization as a velocity-dependent viscosity, just as the Papanastasiou[27] regularization is a shear-stress-dependent viscosity. In this spirit the isotropic regularization of Eq. (12) is

$$u\left[1 + Rb \frac{\tanh(cq/Rb)}{q}\right] = -p_x,$$

(17)

$$w\left[1 + Rb \frac{\tanh(cq/Rb)}{q}\right] = -p_z + Ra\,\theta,$$

(18)

where $q^2 = u^2 + w^2$. The pressure may now be eliminated from between Eqs. (17) and (18) by first introducing the streamfunction, $\psi$,

$$u = -\psi_z, \qquad w = \psi_x, \tag{19}$$

which satisfies Eq. (11), and by cross-differentiation:

$$\nabla^2 \psi + \frac{Rb \tanh(cq/Rb)}{q^3} \left[ \psi_z^2 \psi_{xx} - 2\psi_x \psi_z \psi_{xz} + \psi_x^2 \psi_{zz} \right]$$
$$+ \frac{c\,\mathrm{sech}^2(cq/Rb)}{q^2} \left[ \psi_x^2 \psi_{xx} + 2\psi_x \psi_z \psi_{xz} + \psi_z^2 \psi_{zz} \right] = Ra\,\theta_x. \tag{20}$$

The fluid speed is now given by,

$$q^2 = \psi_x^2 + \psi_z^2. \tag{21}$$

The heat transport equation, (13), transforms to the familiar form,

$$\theta_t + \psi_x \theta_z - \psi_z \theta_x = \theta_{xx} + \theta_{zz}. \tag{22}$$

Finally, the upper and lower boundary conditions are that

$$\psi = 0, \quad \theta = 1 \quad \text{on} \quad z = 0; \qquad \psi = 0, \quad \theta = 0 \quad \text{on} \quad z = 1, \tag{23}$$

while the sidewall conditions are that,

$$\psi = 0, \quad \theta_x = 0 \quad \text{on} \quad x = 0, A. \tag{24}$$

We note that the boundary conditions at $x = 0, A$ are also those which correspond to an internal cell boundary, and therefore these conditions are representative of an infinitely wide cavity, and the cavity itself may possibly contain one cell or more.

Given that regularization plays such a central role here, it is important to comment on two recent papers by Kefayati[28,29] which consider thermosolutal convection of a Bingham fluid in a porous cavity. The regularization used in those papers is the one by Papanastasiou[27] which applies for clear fluids and which is very different from the present one. In these two papers it has been assumed that the Darcy-Brinkman-Forchheimer equations, which correspond to Newtonian flow in a porous medium, may be modified in the same way as the Navier-Stokes equations are to account for the presence of a yield threshold. Thus the diffusion terms are altered from their Newtonian form to account for the Bingham rheology by the use of the appropriate form of the stress tensor; see Eq. (2.2) in Zhang et al.[1], for example. Subsequently the Papanastasiou[27] regularization is applied to those diffusion terms. One consequence of this is that regions of unyielded flow are not necessarily stationary, something which cannot happen in practice because of the presence of pores or particles. In other words, the motion of a Bingham fluid within a porous matrix is dominated by the microstructure of the medium, and the type of averaging which was used in Nash and Rees[26] demonstrates that the macroscopic effect is the existence of a threshold body force that modifies Darcy's law, and not the Brinkman terms.

## D. Numerical approximation.

We have used standard second-order accurate central differences to approximate Eqs. (20) and (22). The Neumann conditions for temperature on the sidewalls were approximated using the fictitious point technique. We employed line-relaxation alternately in each direction with Successive over-relaxation (SOR) to converge to the steady state. A small value (typically 1.2) of the relaxation factor was used to try to speed up the computations a little, but larger values caused oscillatory nonconvergence. The original intent was to use the Full Approximation Scheme multigrid to improve iterative convergence, but it was found that even a two-level implementation was not always reliable and therefore we elected to use SOR in all cases even though convergence to the steady-state was slow when compared with that for a Newtonian fluid. However, the multigrid code which was developed was used with just one grid because the presence of a subroutine to compute residuals meant that we could assess the accuracy of solutions in a manner that was independent of the speed of convergence of the iterations. Convergence was deemed to have taken place once the maximum residual became smaller than $10^{-5}$, and this corresponds to about four significant figures in our computations.

In Eq. (20) the values $q^2$ and $q^3$ appear in the denominators of two terms, and these could cause round-off error to become very large when $q$ is small. This possibility was circumvented by the use of a Taylor's series approximation to the tanh and sech$^2$ terms whenever $q < 10^{-3}$. In such cases we used the following version of Eq. (20),

$$\left[ 1 + c \left\{ 1 - \frac{1}{3} \left( \frac{cq}{Rb} \right)^2 + \frac{2}{15} \left( \frac{cq}{Rb} \right)^4 - \frac{17}{315} \left( \frac{cq}{Rb} \right)^6 \right. \right.$$
$$\left. \left. + \frac{62}{2835} \left( \frac{cq}{Rb} \right)^8 + \cdots \right\} \right] \nabla^2 \psi$$
$$+ \frac{c^3}{Rb^3} \left[ -\frac{2}{3} + \frac{8}{15} \left( \frac{cq}{Rb} \right)^2 - \frac{34}{105} \left( \frac{cq}{Rb} \right)^4 + \frac{496}{2835} \left( \frac{cq}{Rb} \right)^6 + \cdots \right]$$
$$\times \left[ \psi_{xx} \psi_x^2 + 2\psi_x \psi_z \psi_{xz} + \psi_{zz} \psi_z^2 \right] = Ra\,\theta_x, \tag{25}$$

which provides a smooth transition between the small-$q$ and large-$q$ cases in double precision Fortran.

We used a uniform $\mathtt{NX} \times \mathtt{NZ}$ grid and the step length in each direction was $1/64$ in all of our computations. Therefore $\mathtt{NZ} = 64$ in all cases, while the cavity aspect ratio ($A = \mathtt{NX}/\mathtt{NZ}$) could then be varied by taking different values of $\mathtt{NX}$. We found that this amount of resolution was more than adequate for cases where $Ra \leq 150$. As in Rees[21] a detailed study was undertaken to determine how large a value could be used for the regularization constant, $c$. For the present grid we found that $c = 30$ always worked well. Smaller values gave slightly different overall rates of heat transfer, while larger values yielded convergence difficulties. One of the main conclusions made in the Appendix of Rees[21] is that larger values of $c$ may only be used reliably with a finer grid.

## III. RESULTS AND DISCUSSION

### A. Some flow patterns and isotherms

We shall set the context for the rest of the paper by presenting typical streamlines and isotherms for strongly nonlinear convection.

Figure 2 illustrates how increasing values of $Rb$ affects convection within a square cavity when $Ra = 150$. For a Newtonian fluid this value of the Darcy-Rayleigh number is just below $4Ra_c$ (i.e. $16\pi^2$), and therefore the flow is sufficiently strong that the isotherms bend into a distinctive S-shape. When $Rb = 2$, the yield threshold is sufficiently weak that the streamlines (continuous) and isotherms (dotted) are hardly affected. Nevertheless, there is a small region of stagnation in the very centre of the cell which is shaded in orange. The boundary of this region corresponds to that fluid speed, $u$, which is the solution of Eq. (16) with $p_x = \pm Rb$, i.e.

$$u + Rb\tanh(cu/Rb) = \pm Rb. \qquad (26)$$

The distance of the orange disks from the $u = 0$ axis in figure 1 show the range of values of $u$ which are deemed to be stagnant from the point of view of plotting streamlines. Given that this is a region of stagnation, both the normal and tangential velocities at its edge will be zero, and hence the derivative of the streamfunction in the direction perpendicular to that edge will also be zero; this may be seen by the increasing distance between the streamlines as the stagnant region is approached.

As $Rb$ increases, the resistance to flow also increases. One by-product of this is an increase in the size of the central stagnant region. Another is the emergence of stagnant regions in all four corners of the cavity. Accompanying this is a weakening of the flow; this cannot be seen in figure 2 by an inspection of the streamlines because 20 equally-spaced intervals have been used in each subfigure, but it may be inferred by the decreasing deformation of the isotherms. Some numerical data corresponding to figure 2 are given in Table 1 where we define the circulation and the Nusselt number to be

$$Q = |\psi|_{max}, \qquad Nu = \frac{1}{A}\int_0^A \frac{\partial\theta}{\partial z}(z = 0)\,dx, \qquad (27)$$

and hence a pure conduction solution corresponds to $Q = 0$ and $Nu = 1$ independently of the aspect ratio of the cavity. Table 1 shows clearly how both $Q$ and $Nu$ decrease as $Rb$ increases.

For a square cavity and for $Ra = 150$, the flow corresponding to $Rb = 11$ represents the largest integer value of $Rb$ for which a convecting solution may be attained. As $Rb$ increases slowly from 11, the flow continues to decrease in strength, but there is a value of $Rb$ beyond which there is a dramatic collapse to the state of no flow — this will be discussed later. In other contexts, such as the sidewall-heated cavity discussed in Rees[21], there is instead a continuous reduction in the strength of the flow down to zero with an accompanying increase in the proportion of the cavity which is stagnant. In this latter scenario, the flow pattern which exists when $Rb$ is just below its critical value consists of a narrow but weak circuit of moving fluid around the boundary of the cavity.

TABLE I. Computed values of $Q$ and $Nu$ for $Ra = 150$ and $k = \pi$ for the given values of $Rb$. Cases shown in red correspond to those presented in figure 2.

| $Rb$ | $Q$ | $Nu$ |
|---|---|---|
| 0 | 7.380 | 3.358 |
| 1 | 7.021 | 3.280 |
| 2 | 6.676 | 3.199 |
| 3 | 6.331 | 3.113 |
| 4 | 5.985 | 3.022 |
| 5 | 5.637 | 2.925 |
| 6 | 5.284 | 2.822 |
| 7 | 4.925 | 2.712 |
| 8 | 4.556 | 2.591 |
| 9 | 4.165 | 2.452 |
| 10 | 3.724 | 2.298 |
| 11 | 3.146 | 2.076 |

TABLE II. Computed values of $Q$ and $Nu$ for $Ra = 150$ and $Rb = 5$ for nine different aspect ratios. Cases shown in red correspond to those presented in figure 3.

| $A$ | NX | $Q$ | $Nu$ | $k/\pi$ |
|---|---|---|---|---|
| $1/2$ | 32 | 3.042 | 2.420 | 2 |
| $5/8$ | 40 | 4.160 | 2.859 | $8/5$ |
| $3/4$ | 48 | 4.843 | 2.967 | $4/3$ |
| $7/8$ | 56 | 5.318 | 2.971 | $8/7$ |
| 1 | 64 | 5.637 | 2.925 | 1 |
| $9/8$ | 72 | 5.838 | 2.846 | $8/9$ |
| $5/4$ | 80 | 5.949 | 2.743 | $4/5$ |
| $11/8$ | 88 | 5.973 | 2.617 | $8/11$ |
| $3/2$ | 96 | 5.917 | 2.464 | $2/3$ |

Figure 3 shows the effect of having three different wavenumbers when $Ra = 150$ and $Rb = 5$. The effect of this changing aspect ratio is small, at least visually. The central slightly elliptical stagnant region changes its orientation, although it increases its size very slightly as the aspect ratio increases. The degrees of deformation of the isotherms appear not to change greatly and therefore another set of data are provided in Table 2 which shows how $Q$ and $Nu$ vary with aspect ratio. In this Table we see that both the circulation and the rate of heat transfer first increase with $A$, but then achieve a maximum and decrease subsequently. This is a property which is shared by a Newtonian fluid.

### B. Weakly nonlinear analysis

The aim of this subsection is to consider in detail the linear and weakly nonlinear theories of the onset of convection using the regularised Pascal model; this will provide an important context for the rest of the paper.

When the velocities are small then the tanh and $sech^2$ terms in Eq. (20) may be replaced by their Taylor's series approximations; only the first two terms need to be retained here in order to achieve the following weakly nonlinear analysis.
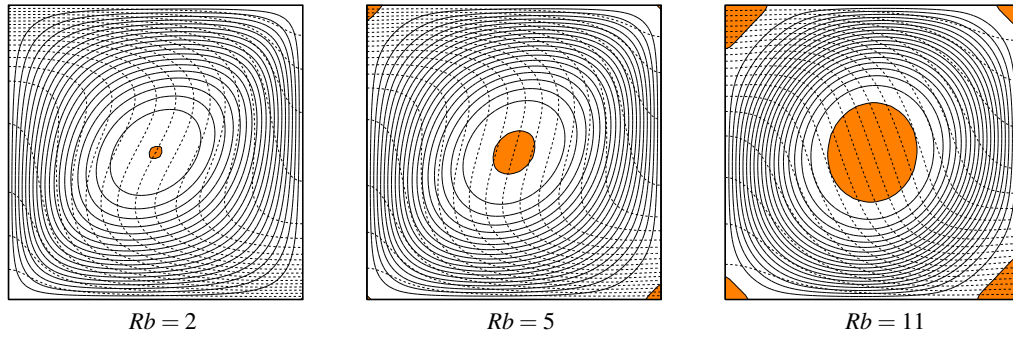
FIG. 2. Showing the streamlines (continuous) and isotherms (dashed) for a unit square with $Ra = 150$ and $c = 30$, and for $Rb$ taking the indicated values. The stagnant regions are shaded in orange. Both the streamlines and isotherms are plotted using 20 equal intervals between their respective extrema; this convention also applies to Fig. 3.
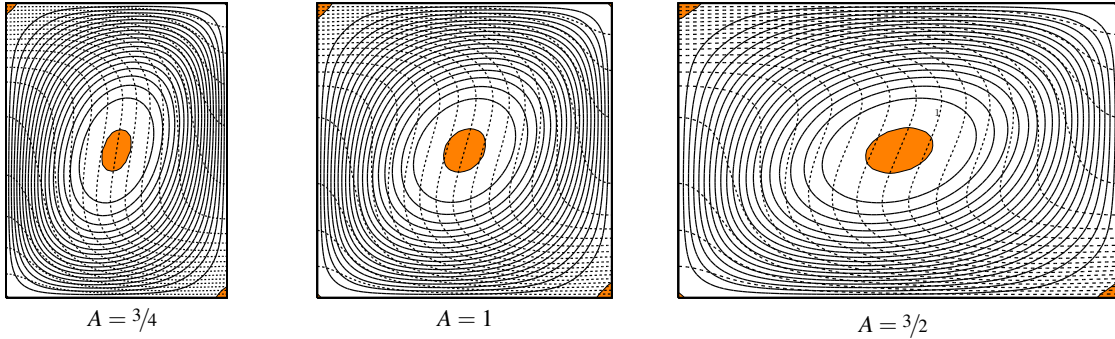


FIG. 3. Showing the streamlines (continuous) and isotherms (dashed) for $Ra = 150$, $Rb = 5$ and $c = 30$, and for the indicated cavity aspect ratios.

Thus Eq. (20) may be replaced by

$$(1+c)\nabla^2\psi - \frac{c^3}{3Rb^2}\left[\psi_x^2 + \psi_z^2\right]\nabla^2\psi$$

$$-\frac{2c^3}{3Rb^2}\left[\psi_{xx}\psi_x^2 + 2\psi_x\psi_z\psi_{xz} + \psi_{zz}\psi_z^2\right] = Ra\,\theta_x. \tag{28}$$

while Eq. (22) remains unchanged. We expand in the usual way:

$$(\psi,\theta) = (0, 1-z) + \varepsilon(\psi_1,\theta_1) + \varepsilon^2(\psi_2,\theta_2) + \cdots, \tag{29}$$

where

$$Ra = Ra_0 + \varepsilon^2 Ra_2 + \cdots, \tag{30}$$

and where the $O(1)$ terms in Eq. (29) represent the motionless conduction state whose stability is being analysed. We shall also replace $t$ by $\frac{1}{2}\varepsilon^2\tau$, a slow time scale, where the $1/2$ is present for numerical convenience.

At leading order we have,

$$(1+c)\nabla^2\psi_1 - Ra_0\theta_{1x} = 0, \tag{31}$$

$$\nabla^2\theta_1 + \psi_{1x} = 0. \tag{32}$$

The solution of this system will be taken to be the onset mode which minimises the critical Darcy-Rayleigh number:

$$\psi_1 = \frac{2}{\pi}A\sin\pi x\sin\pi z, \qquad \theta_1 = \frac{1}{\pi^2}A\cos\pi x\sin\pi z, \tag{33}$$

and

$$Ra_0 = 4(1+c)\pi^2, \tag{34}$$

where $A = A(\tau)$ and where the constants have been chosen so that all the terms in the resulting amplitude equation have unit coefficients when the fluid is Newtonian. The solutions given in Eq. (33) have a horizontal wavenumber which is equal to $\pi$, and therefore each cell occupies a unit square.

At second order in $\varepsilon$ we have the equations,

$$(1+c)\nabla^2\psi_2 - Ra_0\theta_{2x} = 0, \tag{35}$$

$$\nabla^2\theta_2 + \psi_{2x} = \frac{1}{\pi}A^2\sin 2\pi z. \tag{36}$$

The solution is

$$\psi_2 = 0, \qquad \theta_2 = -\frac{1}{4\pi^3}A^2\sin 2\pi z. \tag{37}$$

At third order the equations are

$$(1+c)\nabla^2\psi_3 - Ra_0\theta_{3x} = -\left(\frac{1}{\pi}Ra_2 A + \frac{20c^3}{3Rb^2}A^3\right)\cos\pi x\sin\pi z$$

$$+ \text{ nonresonant terms}$$

$$\equiv \mathscr{R}_1, \tag{38}$$

$$\nabla^2 \theta_3 + \psi_{3x} = \frac{1}{2\pi^2}\left(A_\tau + A^3\right)\cos\pi x \sin\pi z$$

$$+ \text{nonresonant terms} \qquad (39)$$

$$\equiv \mathscr{R}_2,$$

where $\mathscr{R}_1$ and $\mathscr{R}_2$ are defined to be the respective right hand sides of Eqs. (38) and (39). A solvability condition may be applied and it may be written in the form,

$$\int_0^2 \int_0^1 \left[\psi_1\mathscr{R}_1 + Ra_0\theta_1\mathscr{R}_2\right] dz\,dx = 0. \qquad (40)$$

Application of this condition yields the amplitude equation,

$$(1+c)A_\tau = Ra_2 A - \left[(1+c) - \frac{10\pi^2 c^3}{3Rb^2}\right]A^3. \qquad (41)$$

Thus when $c = 0$, the Newtonian case, the above reduces to

$$A_\tau = Ra_2 A - A^3, \qquad (42)$$

and therefore the onset of convection is clearly supercritical because the coefficient of $A^3$ is negative. When $c \gg 1$ in Eq. (41) the coefficient of $A^3$ is positive, and therefore the onset of convection is subcritical. The transitional case arises when the coefficient of $A^3$ is zero. This happens when

$$Rb = \sqrt{\frac{10}{3}\frac{\pi^2 c^3}{(1+c)}}. \qquad (43)$$

If we choose $Rb = 5$ as a representative value then the transition between supercritical and subcritical onset occurs when $c = 1.183954$. The form taken by the Landau equation given in (41) is identical to that derived by Balmforth and Rust[30] in their analysis of a weakly viscoplastic Bénard problem.

Although we shall be presenting representative nonlinear computations in the next subsection, figure 4 displays how the variation of $Q$ with $Ra$ varies as the regularization constant increases from zero. This case uses $Rb = 5$.

When $c = 0$ the fluid is Newtonian and the bifurcation from the zero-flow state takes place at $Ra = Ra_c = 4\pi^2$. The bifurcation is supercritical, and $Q$ begins to rise in a manner which is proportional to $(Ra - Ra_c)^{1/2}$. As $c$ increases from zero, the value of $Ra$ at which onset takes place also increases and it does so in a manner which is given precisely by the value for $Ra_0$ given in Eq. (34). When $c = 1.25$ the computed solution curve terminates above the $Q = 0$ axis, which is above the value of 1.183954 that marks the transition from the bifurcation being supercritical to being subcritical when $Rb = 5$. Thus we infer that there will be a solution branch corresponding to unstable solutions which connects the fold bifurcation, marked by the black disk, and the point of subcritical onset, marked by the circle. The dashed line is a sketch of the qualitative shape taken by that unstable solution branch.

As $c$ increases still further, we see that the stable solution branches and the turning points converge towards a limit (although we also have the aforementioned convergence difficulties when $c$ takes values which are too large). Clearly, the value of $Ra$ at linear onset becomes infinitely large as
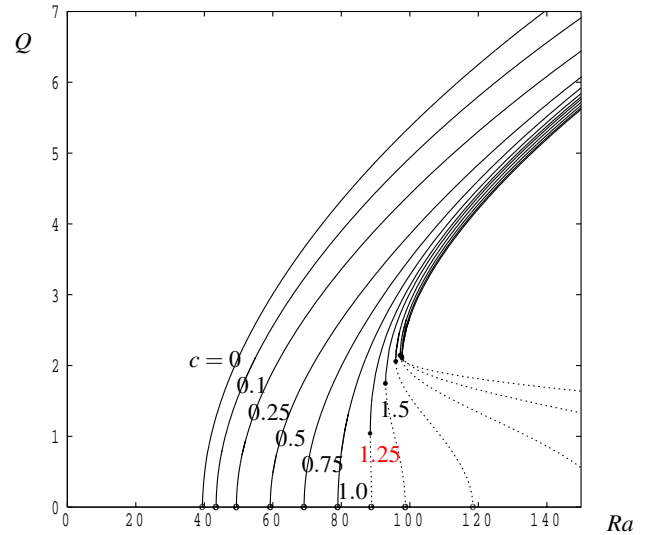


FIG. 4. The variation of $Q$ with $Ra$ for different values of the regularization constant, $c$. The aspect ratio of the cavity is $A = 1$. Continuous lines correspond to steady nonlinear solutions while dashed lines display cubic curves which have been fitted between the turning point (black disks) and the point of linear onset (circles) in order to illustrate the qualitative shapes of the unstable solution branches.

$c \to \infty$, and thus the depth of subcriticality also increases without limit. The evidence adduced so far suggests that the pure Pascal model gives rise to two solution branches, neither of which touches the line $Q = 0$. The use of an entirely different numerical scheme, one which can compute unstable branches, will now need to be used to confirm this conclusion definitively.

## C.  Nonlinear convection

The streamline and isotherm patterns which have been shown in figure. 2 and 3 are representative of all cases for which $Ra \le 150$. There are no cases for which a gradual reduction in the value of $Ra$ or a gradual increase in $Rb$ will lead to a smooth approach to full stagnation. Therefore we shall not present further figures of this kind. Rather, we shall concentrate on the determination of how the Nusselt number, in particular, varies with the governing nondimensional parameters, $Ra$, $Rb$ and $A$ (or the equivalent wavenumber, $k$). In practice it is difficult to find suitable profiles for initial iterates near the fold bifurcation, and therefore our general procedure was first to compute a solution either for a large value of $Ra$ or for a small value of $Rb$, and then either to reduce $Ra$ or to increase $Rb$ gradually, and by taking the previously-computed solution as the initial iterate for the next. The increments in these parameters were chosen so that the change in $Nu$ was controlled, and therefore the fold bifurcations could be approached quite closely. The locations of these points were then obtained *a posteriori* by fitting a suitable quadratic to the final three data points.

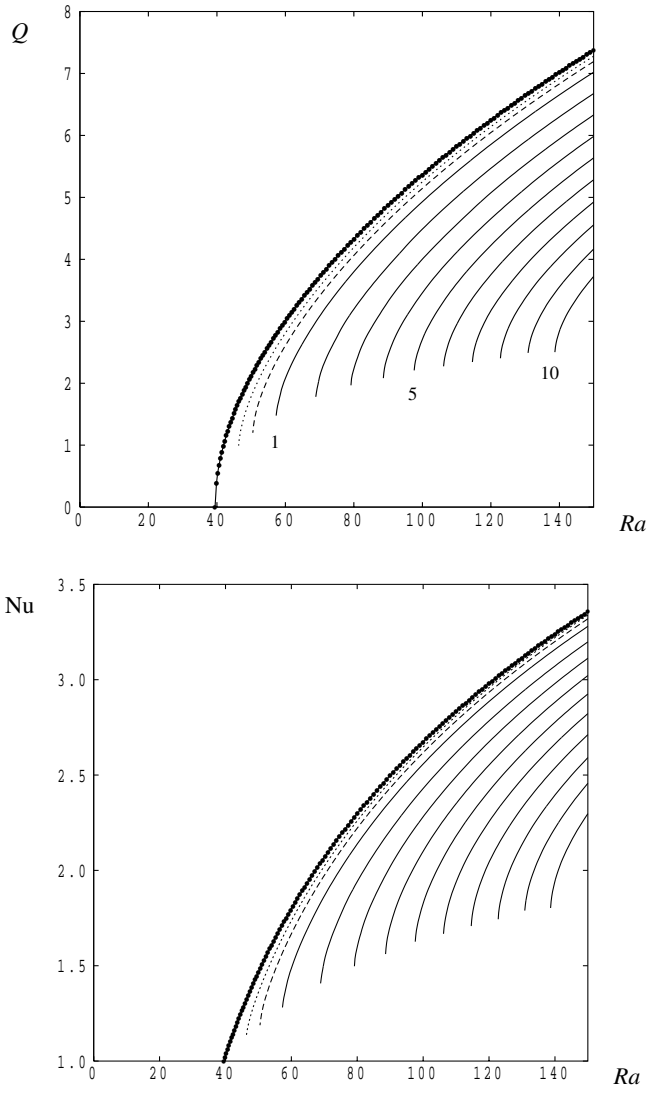Figure 5 shows how both $Q$ and $Nu$ vary with $Ra$ for some

FIG. 5. Variation of $Q$ and Nu with $Ra$ for $Rb = 0, 0.25, 0.5, 1, 2, \cdots$ 10, with $c = 30$ and $A = 1$. The dashed line corresponds to $Rb = 0.5$ and the dotted line to $Rb = 0.25$. The bullets on the $Rb = 0$ curve show the individual computations.
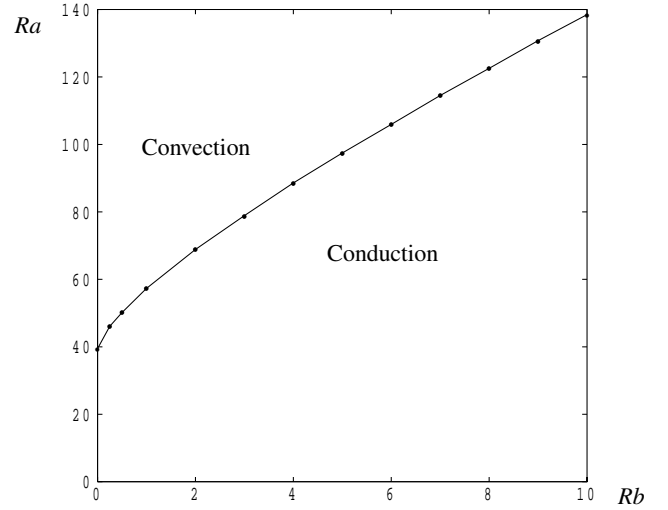


FIG. 6. Showing the variation with $Rb$ of the value of $Ra$ above which strongly nonlinear convection exists. The cavity has a unit aspect ratio. Black disks indicate the computed data points.
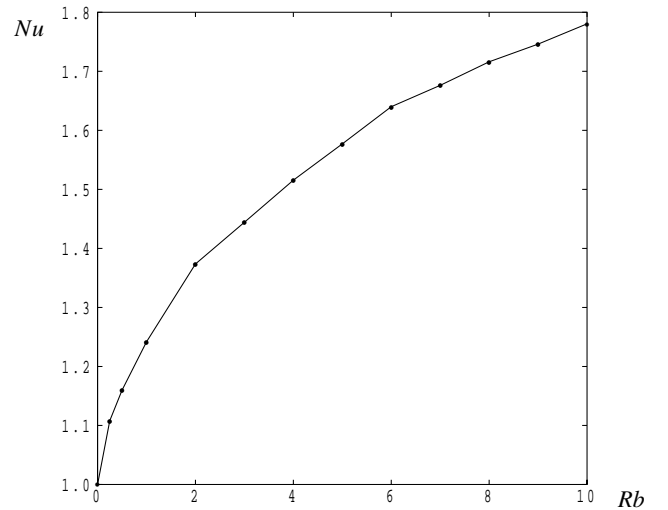


FIG. 7. Showing how the Nusselt number corresponding to flow at the fold bifurcation varies with $Rb$.

chosen values of $Rb$ within a square cavity. For a fixed value of $Rb$ both quantities increase with $Ra$ because of the increasing buoyancy forces, while for a fixed value of $Ra$ both decrease as $Rb$ increases because of the decreasing ability of buoyancy to overcome the yield threshold. We also find that the value of $Ra$ at which strongly nonlinear convection appears also increases with increasing values of $Rb$, and the variation of this critical value of $Ra$ is shown in figure 6. This line is the locus of the fold bifurcation in $(Rb, Ra)$-space for a square cavity. We also see that it approaches $4\pi^2$ as $Rb \to 0$, which is the Newtonian limit. In this Newtonian limit, the strength of the flow which corresponds to the fold bifurcation also decreases towards zero; this is illustrated in figure 7 which displays the Nusselt number as a function of $Rb$. Here $Nu \to 1$ as $Rb \to 0$.

Finally we relax the restriction of having a cavity with a unit aspect ratio. For three different values of $Rb$ figure 8 shows how $Nu$ varies with wavenumber for chosen values of $Ra$; in all of these computations the cavity contains only one cell and therefore the wavenumber satisfies, $k = \pi/A$.

We concentrate first on the Newtonian case, $Rb = 0$. These curves are in very close agreement with those obtained by the present author using a spectral method, and this provides some further corroboration that the present code is error-free. For $Ra = 100$ the present computation also gives very good agreement with the curve shown in de la Torre Juárez and Busse[31]. For each value of $Ra$ there is a wavenumber which maximises the rate of heat transfer, a fact which is consistent with the stability analysis of Straus[32] in which the range of wavenumbers for which convection is stable also drifts towards larger wavenumbers as $Ra$ increases.
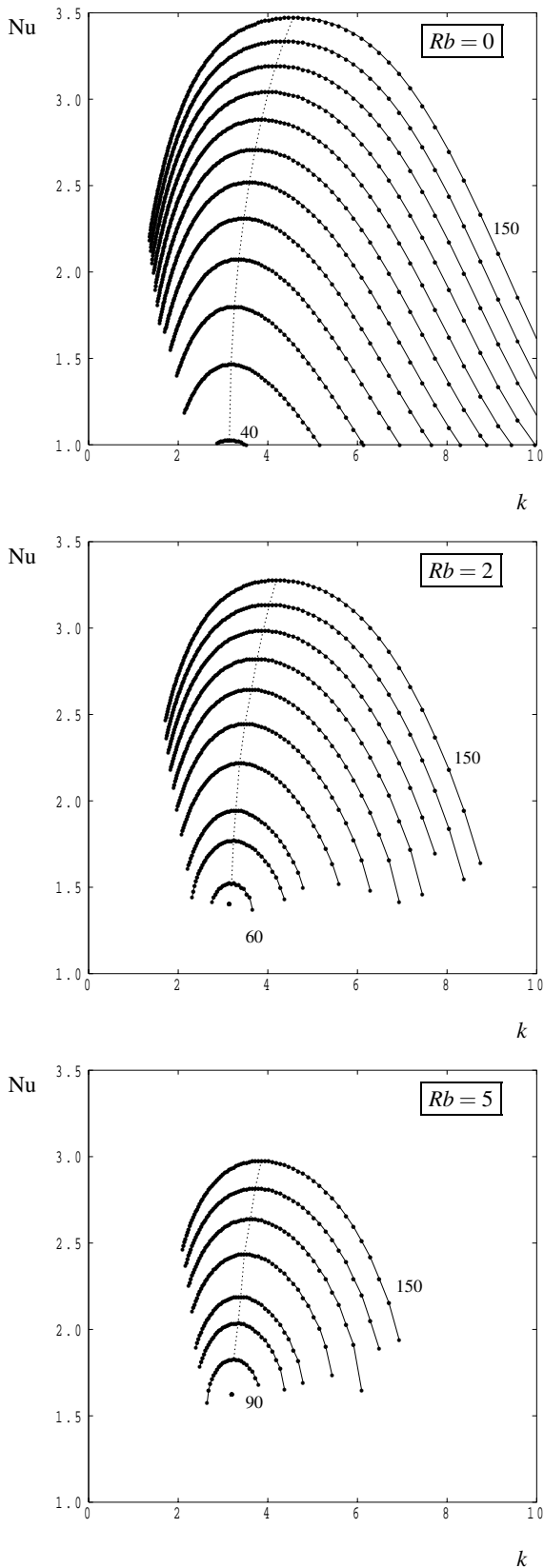
FIG. 8. Variation of Nu with wavenumber, $k$, for the given values of $Ra = 150, 140, 130, 120, \cdots$. The disks on the curves represent each computation undertaken. The dotted line indicates the maximum rate of heat transfer. The single black disks represent the first appearance of nonlinear convection as $Ra$ increases.

It is interesting to note that, as the wavenumber increases, we were able to compute values of $Nu$ all the way to when convection ceases according to linearised theory. However, as the wavenumber decreases, the curves terminate before reaching $Nu = 1$ because the computed flow then becomes unstable to disturbances with three times the wavenumber, a mode shape which shares the same symmetries as the one-cell solutions and which is also present as a component of the one-cell solution.

When $Rb$ takes nonzero values we see again and immediately that the strength of convection decreases but that the value of $Ra$ above which nonlinear convection exists increases. Given our earlier weakly nonlinear analysis, the curves shown for $Rb = 2$ and $Rb = 5$ cannot reach the $Nu = 1$ line and therefore there will be unstable branches like those shown in figure 4 when $c$ is large. Together with the displayed stable branches these will form a closed loop. The detailed behaviour of such loops for small wavenumbers may perhaps be complicated by the instability described in the previous paragraph, but for cases such as $Rb = 5$ and $Ra = 90$ (see figure 8) the loop will be close to being elliptical in shape.

For both $Rb = 2$ and $Rb = 5$, the maximum rate of heat transfer is again attained for an increasing wavenumber as $Ra$ increases. However, as $Ra$ decreases, the optimum wavenumber returns to being at least quite close to $\pi$. The solitary black disks represent an extrapolation back to when nonlinear convection first appears as $Ra$ increases; this may be regarded as a nonlinear isola point.

## IV. CONCLUSIONS

When a yield stress fluid saturates a porous medium and when a uniform layer of such a porous medium is heated from below, then the presence of an $O(1)$ yield threshold means that the no-flow conducting state is linearly stable. The weakly nonlinear analysis of the regularised Pascal model also suggests strongly that the solution curves for the convection of a pure Bingham fluid will, for sufficiently small values of the Darcy-Rayleigh number, be comprised of two branches, one stable and one unstable, and that convection first appears as a strongly convecting motion via a fold bifurcation.

Clearly, if $Rb$ takes any positive value no matter how small, then formally the basic state remains linearly stable and will remain so in the Newtonian limit as $Rb \rightarrow 0$ even though the Newtonian Darcy-Bénard problem itself does undergo linear instability. The resolution of this apparently singular behaviour is that the point of nonlinear onset approaches $Ra = 4\pi^2$ as $Rb \rightarrow 0$ (see figure 6), and that the corresponding amplitude of convection tends to a zero limit (see figure 7 where $Nu \rightarrow 1$, which is characteristic of conduction rather than of convection).

At this stage it is not known how the steady two-dimensional flows presented here will undergo their secondary bifurcations. For a Newtonian fluid, Straus[32] quotes $Ra = 380 \pm 5$ as the Darcy-Rayleigh number above which no steady two-dimensional flow is stable. This corresponds to a cross-roll instability and it is assumed that the resulting

pattern will then be three-dimensional. At this limit of stability the wavenumber may be estimated to be roughly 8.1 from figure 4 in Straus[32], as compared with $\pi$ at onset. Given that the presence of a yield threshold serves to reduce the magnitude of convection it may be predicted that steady two-dimensional Darcy-Bingham-Bénard convection may remain stable to small-amplitude disturbances at larger values of the Darcy-Rayleigh number. However, the later analysis by Riley and Winters[33] found that steady two-dimensional convection with $k = \pi$ loses its stability at a Hopf bifurcation when $Ra = 390.7$, a value which is very close to that of Straus, but with a very different wavenumber. Riley and Winters[33] also show that it is possible to have unsteady flow when $Ra$ is as small as roughly 250 when $A = 2.5$ (i.e. $k = 1.26$); this appears not to be the result of a linear instability of a steady state, but was determined by the use of a curve-tracking algorithm and therefore will be realised in practice via a large-amplitude perturbation of a steady convecting state. We think it highly unlikely that the presence of a Bingham fluid can induce a persistently unsteady convection when $Ra \leq 150$ given that the yield threshold serves to reduce the effectiveness of buoyancy forces to cause convective flow.

## DATA AVAILABILITY STATEMENT

## REFERENCES

[1] J. Zhang, D. Vola, and I. A. Frigaard, "Yield stress effects on Rayleigh-Bénard convection," J.Fluid Mech. **566**, 389–419 (2006).

[2] M. Darbouli, C. Métivier, J. P. Piau, A. Magnin, and A. Abdelali, "Rayleigh-Bénard convection for viscoplastic fluids," Physics of Fluids **25(2)**, 104102 (2013).

[3] Z. Kebiche, C. Castelain, and T. Burghelea, "Experimental investigation of the Rayleigh-Bénard convection in a yield stress fluid," J. Non-Newtonian Fluid Mech. **203**, 9–23 (2014).

[4] C. Metivier, C. Li, and A. Magnin, "Origin of the onset of Rayleigh-Bénard convection in a concentrated suspension of microgels with a yield stress behavior," Physics of Fluids **29(10)**, 6619–6644 (2017).

[5] O. Turan, N. Chakraborty, and R. J. Poole, "Laminar Rayleigh-Bénard convection of yield stress fluids in a square enclosure," J. Non-Newtonian Fluid Mech. **171**, 83–96 (2012).

[6] O. Turan, R. J. Poole, and N. Chakraborty, "Influences of boundary conditions on laminar natural convection of Bingham fluids in rectangular enclosures with differentially heated side walls," Heat Transfer Engineering **35 (9)**, 822–849 (2014).

[7] O. Turan, S. Yigit, and N. Chakraborty, "Critical condition for Rayleigh-Bénard convection of Bingham fluids in rectangular enclosures," Int. Comm. Heat Mass Transfer **86**, 117–125 (2017).

[8] S. Yigit, S. Chen, P. Quinn, and N. Chakraborty, "Numerical investigation of laminar Rayleigh-Bénard convection of Bingham fluids in square cross-sectioned cylindrical enclosures," Int. J. Thermal Sciences **110**, 356–368 (2016).

[9] S. Yigit and N. Chakraborty, "Influences of aspect ratio and wall boundary condition on laminar Rayleigh-Bénard convection of Bingham fluids in rectangular enclosures," Int. J. Numerical Methods Heat Fluid Flow **27(2)**, 310–333 (2017).

[10] S. Yigit and N. Chakraborty, "Numerical investigation of aspect ratio influences on Rayleigh-Bénard convection of Bingham fluids in vertical cylindrical annuli," Int. J. Numerical Methods Heat Fluid Flow **29(1)**, 251–279 (2019).

[11] D. A. S. Rees, "On convective boundary layer flows of a Bingham fluid in a porous medium," Int. J. Heat Mass Transfer **82**, 206–212 (2015).

[12] D. A. S. Rees and A. P. Bassom, "Unsteady thermal boundary layer flows of a Bingham fluid in a porous medium," Int. J. Heat Mass Transfer **82**, 460–467 (2015).

[13] D. A. S. Rees and A. P. Bassom, "Unsteady thermal boundary layer flows of a Bingham fluid in a porous medium following a sudden change in surface heat flux," Int. J. Heat Mass Transfer **93**, 1100–1106 (2016).

[14] D. A. S. Rees and A. P. Bassom, "Unsteady free convection boundary layer flows of a Darcy-Bingham fluid in cylindrical cavities," Transport in Porous Media **127(3)**, 711–728 (2019).

[15] D. A. S. Rees and A. P. Bassom, "The effect of internal and external heating on the free convective flow of a Bingham fluid in a vertical porous channel," Fluids (MDPI) **4(2)**, (15 pages) (2019).

[16] W. J. Yang and H. C. Yeh, "Free convective flow of Bingham plastic between two vertical plates," J. Heat Transfer **87(2)**, 319–320 (1965).

[17] J. Kleppe and W. J. Marner, "Transient free convection in a Bingham plastic on a vertical flat plate," J. Heat Transfer **94(4)**, 371–376 (1972).

[18] N. Patel and D. B. Ingham, "Analytic solutions for the mixed convection flow of non-Newtonian fluids in parallel-plate ducts," Int. Comm. Heat Mass Transfer **21(1)**, 75–84 (1994).

[19] Y. Bayazitoglu, P. R. Paslay, and P. Cernocky, "Laminar Bingham fluid flow between vertical parallel plates," Int. J. Thermal Science **46**, 349–355 (2007).

[20] A. Barletta and E. Magyari, "Buoyant Couette-Bingham flow between vertical parallel plates," Int. J. Thermal Sciences **47**, 811–819 (2008).

[21] D. A. S. Rees, "The convection of a Bingham fluid in a differentially-heated porous cavity," Int. J. Num. Methods Heat Fluid Flow **26**, 879–896 (2016).

[22] H. Pascal, "Nonsteady flow through porous media in the presence of a threshold gradient," Acta Mechanica **39**, 207–224 (1981).

[23] E. Buckingham, "On plastic flow through capillary tubes," Proceedings American Society for Testing Materials **21**, 1154–1156 (1921).

[24] M. Reiner, "Ueber die Strömung einer elastischen Flüssigkeit durch eine Kapillare. Beitrag zur Theorie Viskositätsmessungen," Colloid and Polymer Science **39**, 80–87 (1926).

[25] E. C. Bingham, "An investigation of the laws of plastic flow," US Bureau of Standards Bulletin **13**, 309–353 (1916).

[26] S. Nash and D. A. S. Rees, "The effect of microstructure on models for the flow of a Bingham fluid in porous media," Transport in Porous Media **116**, 1073–1092 (2017).

[27] T. C. Papanastasiou, "Flow of materials with yield," Journal of Rheology **31**, 385–404 (1987).

[28] Gh. R. Kefayati, "Lattice Boltzmann simulation of double-diffusive natural convection of viscoplastic fluids in a porous cavity," Physics of Fluids **31**, 013105 (2019).

[29] Gh. R. Kefayati, "Thermosolutal natural convection of viscoplastic fluids in an open porous cavity," Int. J. Heat Mass Transfer **138**, 401–419 (2019).

[30] N. J. Balmforth and A. C. Rust, "Weakly nonlinear viscoplastic convection," J. Non-Newtonian Fluid Mech. **158**, 36–45 (1982).

[31] M. de la Torre Juárez and F. H. Busse, "Stability of two-dimensional convection in a fluid-saturated porous medium," J. Fluid Mech. **292** (1995).

[32] J. M. Straus, "Large amplitude convection in porous media," J. Fluid Mech. **64**, 51–63 (1974).

[33] D. S. Riley and K. H. Winters, "Time-periodic convection in porous media: the evolution of Hopf bifurcations with aspect ratio," J. Fluid Mech. **223**, 457–474 (1991).